Optimizing Nanocomposites through Nanocrystal Surface Chemistry: Superconducting $YBa_2Cu_3O_7$ Thin Films via Low-Fluorine Metal Organic Deposition and Preformed Metal Oxide Nanocrystals.

Hannes Rijckaert[†], *Glenn Pollefeyt*[†], *Max Sieger*[‡], *Jens Hänisch*[§], *Jan Bennewitz*[|], *Katrien De Keukeleere*[†], *Jonathan De Roo*[†], *Ruben Hühne*[‡], *Michael Bäcker*[|], *Petriina Paturi*[⊥], *Hannu Huhtinen*[⊥], *Maximilian Hemgesberg*[□] *and Isabel Van Driessche*[†,*]

[†] Ghent University, SCRiPTS, Dep. of Inorganic and Physical Chemistry, Krijgslaan 281-S3, 9000 Ghent, Belgium

[‡] IFW Dresden, Institute for Metallic Materials, Helmholtzstraße 20, 01069 Dresden, Germany

[§] Karlsruhe Institute of Technology, Institute for Technical Physics, Hermann-von-Helmholtz-Platz 1, 76344 Eggenstein-Leopoldshafen, Germany

[|] Deutsche Nanoschicht GmbH, Heisenbergstraße 16, 53359 Rheinbach, Germany

[⊥] University of Turku, Wihuri Physical Laboratory, Dep. of Physics and Astronomy, 20014 Turku, Finland

[□] BASF SE, Advanced Materials & Systems Research, Carl-Bosch-Straße 38, 67056, Ludwigshafen am Rhein, Germany

Keywords: chemical solution deposition, low-fluorine YBCO, ex-situ nanocomposite, nanoparticles, vortex pinning

Abstract

Achieving low cost, safe, reproducible and high performance superconducting thin films of $YBa_2Cu_3O_{7-\delta}$ is essential to bring this material to the energy market. Here, we report on the chemical solution deposition of $YBa_2Cu_3O_{7-\delta}$ nanocomposites from environmentally benign precursors with a low-fluorine content. Preformed ZrO_2 nanocrystals (3.5 nm) were stabilized in a methanolic precursor solution via two strategies: charge stabilization and steric stabilization. Counter-intuitively, charge stabilization did not result in high quality superconducting layers, while the steric stabilization resulted in highly reproducible nanocomposite thin films with a self-field J_c of 4-5 MA cm^{-2} (77 K) and a much smaller decay of J_c with magnetic field compared to $YBa_2Cu_3O_{7-\delta}$ without nanocrystals. In addition, these nanocomposite films show a strong pinning force enhancement and a reduced J_c anisotropy compared to undoped $YBa_2Cu_3O_{7-\delta}$ films. Given the relationship between the nanocrystal surface chemistry and final nanocomposite performance, we expect these results to be also relevant for other nanocomposite research.

Introduction

Coated conductors based on high-temperature superconducting $YBa_2Cu_3O_{7-\delta}$ (YBCO) films have the potential to change the paradigm in large-scale energy applications due to their moderate cooling requirements, unique efficiency and low weight/size.[1] Electric power applications such as motors and generators, require engineering critical current densities of 30 to 40 kA cm^{-2} at 55 to 65 K in operating fields of 3 to 5 T.[2] Unfortunately, YBCO films typically exhibit a strong reduction of the critical current density (J_c) with increasing magnetic field strength caused by vortex motion.[3] The incorporation of nano-sized defects has proven to be an effective approach to achieve the immobilization of vortices, i.e. flux pinning. Besides rare-earth substitution[4], irradiation[5], template modification[6] and optimizing natural growth defects[7], the introduction of nanoparticles or even self-aligned nanocolumns was achieved via pulsed laser deposition and metal-organic chemical vapour deposition. These so-called artificial pinning centres can be introduced in different dimensions and shapes, preventing the drastic decrease of J_c at moderate-to-high magnetic fields as well as its anisotropy with respect to the magnetic field direction.[8] Nanocolumns for example effectively pin the vortices especially at the magnetic field parallel to the YBCO *c*-axis.[9-13]

In recent years, significant advances in chemical solution deposition (CSD) of both buffer layer architecture and superconducting layer have shown the potential of CSD-based superconductors for a wide range of technological applications.[14-16] Typically, a precursor solution, containing yttrium, barium and copper trifluoroacetates, is successively deposited, pyrolyzed and crystallized into $YBa_2Cu_3O_{7-\delta}$ thin films (Figure 1). This solution approach offers a less expensive route to the coated conductors design, being more scalable and faster compared to vacuum deposition methods. CSD has explored the fabrication of nanocomposite thin films with the formation of effective artificial pinning centres by the addition of excess metal salts to the YBCO precursor solution, resulting in the spontaneous segregation of non-

superconducting secondary phases such as Y_2O_3, $BaSnO_3$, $BaHfO_3$, $BaZrO_3$ and Ba_2YTaO_6.[17-22] However, this approach offers limited control on the formation and size distribution of the nanostructures and faces issues with reproducibility. To reproducibly gain control over the final microstructural properties of the nanocomposite thin films, we opted to synthesize colloidally stable nanocrystals in advance and add them to the YBCO precursor solution (Figure 1, stage I). Up to now, only a few attempts have been made at nanocomposites using preformed nanocrystals (Au, CeO_2 and ZrO_2)[23-25] and the success has been limited because the nanocrystals are either pushed to the YBCO surface or accumulated at the substrate interface. The latter hampers the epitaxial growth of YBCO, leading to poor superconducting properties.[24]

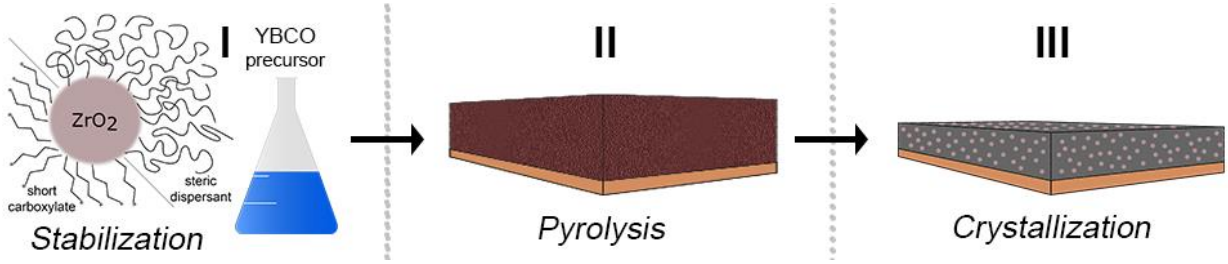

Figure 1. Schematic illustration (not scaled) of the procedure for fabricating YBCO-nanocrystals nanocomposite. The process begins with (Stage I) the stabilization of nanocrystals with a steric dispersant or short carboxylate in the YBCO precursor solution. (Stage II) Deposition of YBCO precursor solution on a single crystalline or technical substrate and its thermal decomposition. (Stage III) The pyrolyzed layer is thermally treated to crystallize YBCO around the nanocrystals.

In addition, YBCO CSD research should evolve towards the use of precursors with lower fluorine content – based on propionates instead of trifluoroacetates – to reduce the release of toxic fluorinated compounds during the thermal process.[26, 27] As such, low-fluorine processes are more environmentally benign and less corrosive, thus better suited for industrial production. However, the corresponding formation of nanocomposites from preformed nanocrystals remains elusive since the developed nanocrystal surface chemistry for the

stabilization in trifluoroacetate-based precursor solutions (pH = 2) is incompatible with the higher pH of the low-fluorine (LF) solution (pH = 6).[24, 25, 28] Therefore, ligand exchange and the appropriate stabilization procedure are important aspects in nanocomposite research. Due to the delicate growth process of textured YBCO layers and poisoning of the superconductor by many chemical elements like metals, halides (except F), sulphur and phosphorus, the restrictions on the final ligand for the preformed nanocrystals are severe.[28]

In this work, we successfully deposit a high quality nanocomposite thin film from low-fluorine precursors and uncover important relations between nanocrystal stabilization and final performance.

Monodisperse 3.5 nm ZrO_2 nanocrystals are synthesized in tri-n-octylphosphine oxide and appear to be capped with hydrophobic ligands after synthesis.[29] These nanocrystals are dispersed in LF-YBCO precursor solutions either with a large steric ligand or a short carboxylate. The nano-suspension precursors – up to 30 mol-% of nanocrystals – are highly stable and have a long shelf-life (>6 month). The 5 mol-% ZrO_2 nano-suspension is spin-coated on $LaAlO_3$ single crystal substrates, pyrolyzed and crystallized. The final superconducting layers reach J_c values up to 5.2 MA cm^{-2} (at 77 K, self-field) with a strong pinning force enhancement due to the optimization of the chosen ligands. The 5 mol-% ZrO_2 nanocomposite is chosen as a model system to study the effect of ligands and preformed nanocrystals on the microstructure and physical properties of the nanocomposite thin films since a higher loading of nanocrystals leads to poor superconducting properties. This comprehensive study can initiate the improvement of many functional and structural properties of nanocomposite thin films in several material classes, including solar cells[30], ferroelectrics[31], multiferroics[32], biosensors[33] and metamaterials[34, 35]. Each of these materials have a huge potential to be refined through microstructure engineering[36, 37].

Results and discussion

ZrO_2 nanocrystals. Spherical ZrO_2 nanocrystals are obtained via the heating-up synthesis using $ZrCl_4$, $Zr(iPrO)_4$.iPrOH and tri-n-octylphosphine oxide, as described by Joo *et al.*[29] The nanocrystals have a cubic crystal structure, confirmed by X-ray diffraction (XRD, Figure 2A). A crystallinity of 85 % was obtained via Rietveld quantitative analysis (Supporting information (SI) for more details). The ZrO_2 nanocrystals are colloidally stable in nonpolar solvents (e.g. toluene), featuring a solvodynamic diameter of 5.9 nm in Dynamic Light Scattering measurements (DLS, Figure 2B). This is consistent with the nanocrystal core diameter of 3.5±0.4 nm (TEM, Figure 2C) and an organic ligand shell of 1.2 nm. The high crystallinity of the ZrO_2 nanocrystals is further corroborated by high resolution (HR) TEM of a ZrO_2 nanocrystal (inset of Figure 2C) where (111) lattice fringes are clearly visible.

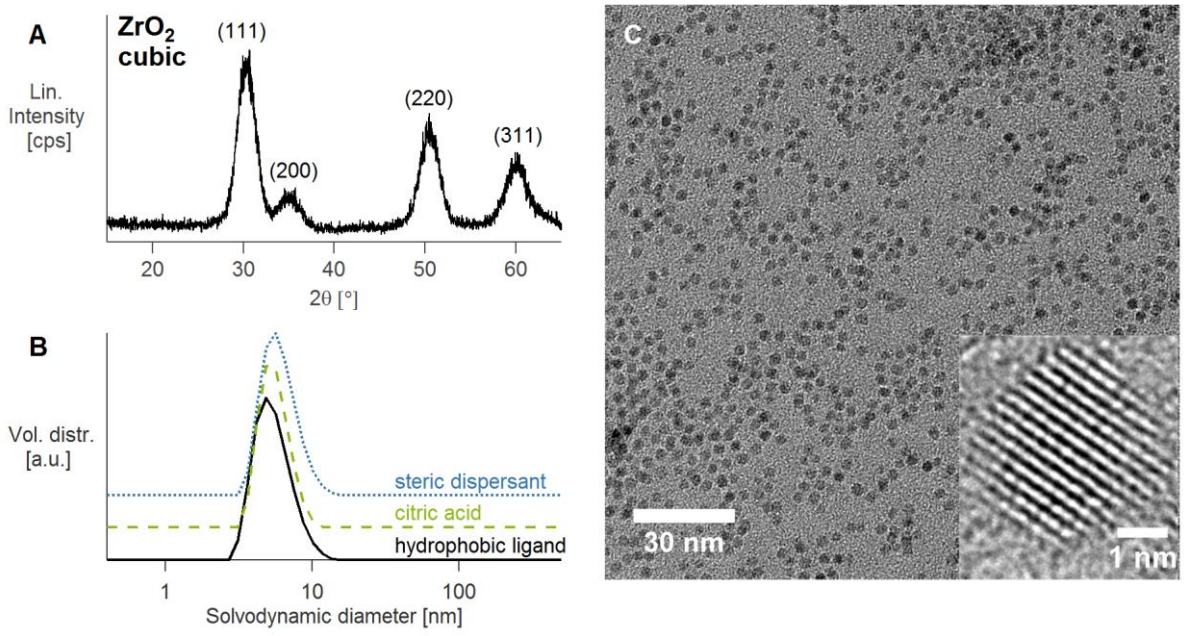

Figure 2. ZrO_2 nanocrystals synthesized in tri-n-octylphosphine oxide: (A) XRD spectrum showing only reflections of the cubic phase. (B) DLS volume percent analysis of ZrO_2 nanocrystals before (black line), after ligand exchange with citric acid (green dashed line) and after ligand exchange with the steric dispersant (blue dotted line). (C) TEM image of the ZrO_2 nanocrystals after heating-up synthesis. The inset shows (111) lattice fringes.

Since the nanocrystals are capped with hydrophobic ligands, a ligand exchange is indispensable for stabilization in the methanol based LF-YBCO precursor solution (Figure 1, stage I).[16, 28] We found that short carboxylic acids (citric acid or tartaric acid) as well as a steric dispersant (a polar copolymer containing a phosphate group, see Figure S2 for the structure) are able to stabilize the ZrO_2 nanocrystals in methanol and in the LF-YBCO precursor solution. DLS analysis (Figure 2B and **Table 1**) confirms the successful ligand exchange and phase transfer to methanol with a solvodynamic diameter of 6.4 nm for the steric dispersant, 5.9 nm for tartaric acid (DLS, Figure S3 in SI) and 5.8 nm for citric acid. It is noteworthy that the colloidal integrity of the copolymer capped nanocrystals is maintained in the highly ionic LF-YBCO precursor solution even at high loadings (up to 30 mol-%), since the solution remains stable for more than six months and no precipitates are observed (Figure S4 in SI). In contrast, citric acid capped nanocrystals (5 mol-%) remain stable for only one week in the LF-YBCO precursor solution. ^{1}H Nuclear Magnetic Resonance (NMR) measurements in methanol-d_4 reveal that the copolymer effectively interacts with the nanocrystal surface as evidenced by negative nOe (nuclear Overhauser effect) cross peaks in the NOESY spectrum (Figure S5A).[38] In DOSY (Diffusion Ordered Spectroscopy) we observe two sets of resonances for the copolymer (Figure S5B). The slowly diffusing species features a diffusion coefficient of 107 $\mu m^2\ s^{-1}$, corresponding to a solvodynamic diameter of 7.5 nm. This is in agreement with the solvodynamic diameter from DLS and we conclude that the copolymer is tightly bound to the nanocrystal. The other set of resonances with a higher diffusion coefficient corresponds to free copolymer. The principle of coordination is the same as for the citric acid or tartaric acid stabilization; the acidic group coordinates to the surface. In comparison to the stabilization with short carboxylates, the steric bulk of the copolymer screens the interaction with other particles more effectively. This is also reflected in the polydispersity index (obtained via DLS analysis, Table 1) which is significantly smaller in the

copolymer stabilized dispersion, indicating a better stabilization. In addition, when the dispersions are drop casted onto TEM grids, the short carboxylate stabilization shows aggregates and individual particles whereas the copolymer stabilization features only individual particles (Figure S6 in SI).

Table 1. Overview of the LF-YBCO nanocomposite precursors with different ligands, their solvodynamic diameter and polydispersity index in methanol and their decomposition temperature of pure ligands, indicating the different critical current densities (self-field, 77 K).

Ligand	d_s **nm**	**Polydispersity index**	T_{decomp} **°C**	$J_{c,sf}$ **(77 K) MA cm^{-2}**
Copolymer	6.4	0.32	340	5.1
Citric acid	5.8	0.86	250	2.3
Tartaric acid	5.9	0.91	265	1.6

Nanocomposite formation and the influence of ligands. After spin-coating of undoped and ZrO_2-doped YBCO precursors on $LaAlO_3$ substrates, the layers were pyrolyzed in a wet O_2 atmosphere (Figure 1, stage II). Optically homogeneous layers were obtained without the formation of defects such as buckling or cracks (SI, Figure S7). In earlier attempts at nanocomposites, the nanocrystals were always stabilized with short ligands such as amino acid (e.g. glutamine), triethyleneglycol or a fatty acid (e.g. decanoic acid).[24, 25] These types of ligands are of same length scale as the short carboxylic acids (citric and tartaric acid) in this work. From thermogravimetric analysis (TGA, Figure S8 in SI and Table 1), we conclude that the short carboxylates decompose at lower temperatures (250 °C for citric acid and 265 °C for tartaric acid) compared to the copolymer which decomposed around 340 °C. The fact that the copolymer is a more thermally stable ligand might prevent early coagulation of the nanocrystals in the pyrolyzing matrix and thus leading to a more homogeneous nanocomposite.

Apart from the stabilization of the nanocrystals, it is important that the ligands do not disturb the decomposition of LF-YBCO precursor itself. The temperature dependence of the decomposition was investigated by TGA analysis (Figure 3A and Figure S9 in SI). The weight loss starts earlier for 5 mol-% nanocrystal addition (at 150 °C) compared to undoped YBCO precursor (at 210 °C). In addition, the nanocomposite precursor with copolymer as ligand shows a slightly slower weight loss between 310 and 340 °C, consistent with the slower decomposition of the pure ligand (*vide supra*). Nevertheless, both undoped and nanocomposite precursors are fully decomposed at 400 °C, indicating the successful pyrolysis of YBCO precursors in the presence of nanocrystals and ligands (both short carboxylates and steric dispersant). The microstructure of the pyrolyzed layers consists of CuO nanoparticles embedded in a matrix of $Ba_{1-x}Y_xF_{2+x}$.[39]

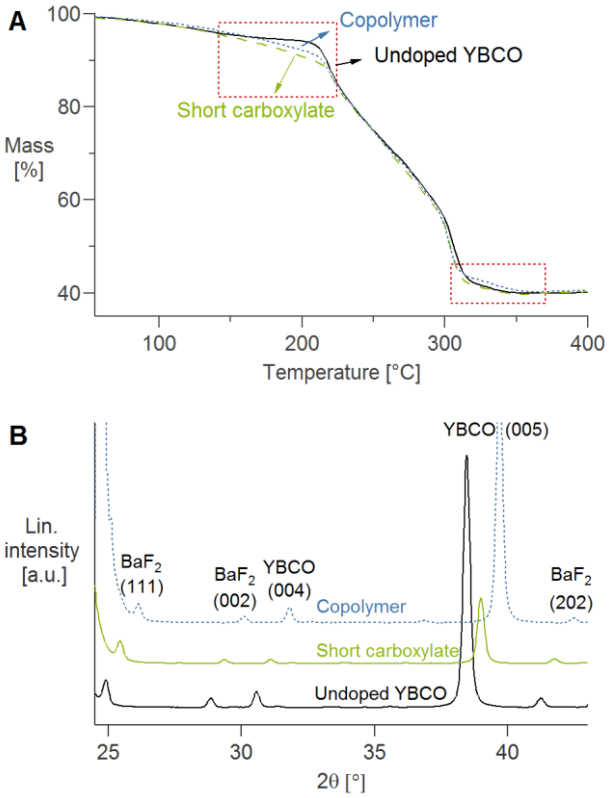

Figure 3. (A) TGA curves of the LF-YBCO nanocomposite precursor with steric dispersant and with short carboxylate in comparison with an undoped LF-YBCO precursor (black line) dried in air atmosphere. More

details of red rectangle marked are shown in SI. (B) XRD scans of different crystallized YBCO films quenched at 790 °C, indicating the YBCO growth rate is different.

After crystallization (Figure 1, stage III), epitaxial YBCO was obtained for all pyrolyzed layers. However, the critical current density of the citric acid and tartaric acid based nanocomposites are only in the range of 1.5-2.5 MA cm^{-2} compared to 4.8 MA cm^{-2} for undoped YBCO, while the copolymer based nanocomposite showed a critical current density of 5.1 MA cm^{-2} (Table 1). Clearly, the nature of the ligands is crucial to the final superconducting performance of the nanocomposite. To study this effect in more detail, we analysed samples that were thermally quenched as soon as they reached the growth temperature of 790 °C. The XRD spectrum (Figure 3B) features crystalline BaF_2 that is in the process of reacting towards epitaxial YBCO. Interestingly, the (005) reflection of YBCO is much lower for the citric acid based nanocomposite, indicating a slower growth rate. We infer that the slow growth rate is symptomatic for poor epitaxial growth, resulting in the lower critical current density. Indeed, the fast decomposition of citric acid can interfere with the drying and/or sintering process of the gel as described by Zalamova *et al.*[40] In this regard, it is also worth noting that amino acid capped ZrO_2 nanocrystals[25] settle on the $LaAlO_3$ interface during pyrolysis of the YBCO trifluoroacetate precursor, resulting in a disturbed epitaxial growth of YBCO. To investigate whether the same mechanism occurs here, X-ray photoelectron spectroscopy measurements were performed on the pyrolyzed films. Interestingly, the ZrO_2 nanocrystals are spread throughout the amorphous matrix for both the copolymer and citric acid based LF-YBCO nanocomposites (SI, Figure S10). Clearly, the behaviour of nanocrystals during pyrolysis depends on their surface chemistry and the YBCO precursor solution. Given the high current density of the copolymer based nanocomposites, we examined the structural quality and superconducting performance of these materials in detail and compared with undoped films.

Optimized copolymer based nanocomposite, a structural investigation. The pyrolyzed layers of undoped YBCO and copolymer based nanocomposites are crystallized at 790 °C after a 1 hour dwell step at 640 °C. This two-step process is used to limit the particle size and therefore to control the microstructure.[22] The surfaces of both undoped YBCO and nanocomposite films are dense and smooth without the presence of any *a*/*b*-oriented grains (Figure 4). Cross-sectional SEM analysis shows that the thickness of the YBCO film is 350-375 nm (inset Figure 4) with minor secondary phases.

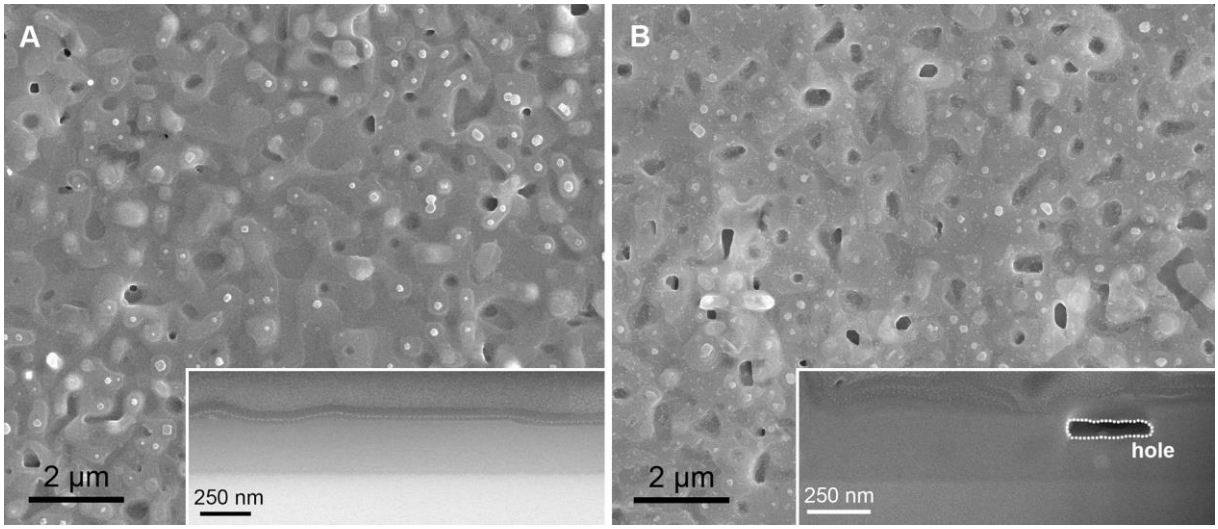

Figure 4. Topographical top-view SEM image of (A) undoped and (B) 5 mol-% ZrO_2 nanocrystals YBCO thin films with cross-sectional side-view as insets.

The YBCO thin films with and without 5 mol-% ZrO_2 nanocrystals exhibit an (00ℓ) texture, that unequivocally proves that the YBCO phase grows epitaxially on the $LaAlO_3$ substrate for both precursors (Figure 5). Small amounts of secondary phases such as $Ba_xCu_yO_z$ – mostly poorly ordered $BaCu_3O_4$ (2θ = 27.7° and 42°)[41] – and Y_2O_3 ((220) at 29.9° and (004) at 34.2°) are detected. The $Ba_xCu_yO_z$ content is reduced for 5 mol-% ZrO_2 nanocrystals, most likely due to reaction of Ba^{2+} with ZrO_2 nanocrystals during the crystallization, which results in a higher fraction of biaxially and randomly oriented Y_2O_3 particles. The latter has also been shown to contribute to vortex pinning.[42, 43] Nanocomposite films show a reflection at 43.0° for

$BaZrO_3$ (200), while ZrO_2 reflections remain absent. This confirms the transformation of the ZrO_2 nanocrystals into $BaZrO_3$ nanocrystals during the heat treatment. The crystallite size of $BaZrO_3$ (200) is 12 nm, calculated via the Scherrer equation. No reflection of YBCO (103) ($2\theta = 32.8°$) can be observed, which would have represented a misoriented fraction.

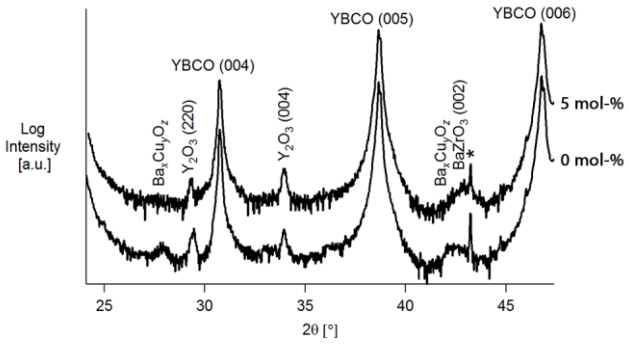

Figure 5. XRD analysis of undoped YBCO and the 5 mol-% ZrO_2- copolymer based nanocomposite after crystallization.

The YBCO (103) pole figures of the samples with and without nanocrystals (Figure S11 in SI) show a fourfold symmetry, demonstrating that the films are biaxially oriented (cube-on-cube relationship). The FWHM values of the YBCO (103) φ-scans (Figure S12 in SI) of undoped YBCO and nanocomposite are about 0.8°, indicating a sharp in-plane alignment. The out-of-plane crystallographic texture of YBCO is determined by measuring the FWHM values of the YBCO (006) XRD rocking curves (ω-scans) (Figure S13 in SI). Undoped samples give 0.43° compared to 0.56° for a nanocomposite film. The widening of the rocking curve can indicate a small increase of microstrain in the nanocomposite.[44] We conclude that the structural integrity of the nanocomposite films is comparable to the undoped YBCO layers.

The fully biaxial (00ℓ) texture of the YBCO layer with cube-on-cube orientation between YBCO and $LaAlO_3$ is further corroborated by the HR-TEM image of the $LaAlO_3$/YBCO interface (Figure 6A) with the electron diffraction pattern as inset. There are no defect

structures in the YBCO matrix around randomly oriented $Ba_xCu_yO_z$ particles visible in the HR-TEM image (Figure 6B) and the FFT pattern (Figure S14A in SI). Figure 6C shows a cross-sectional STEM image of undoped YBCO with $Ba_xCu_yO_z$ and Y_2O_3 particles embedded in the YBCO layer, which is in agreement with the XRD analysis (Figure 5). In the nanocomposite, $BaZrO_3$ particles are mainly homogenously dispersed throughout the film, although some are present at the interface (black dots in Figure 6D). An isolated, randomly oriented $BaZrO_3$ particle is shown in Figure 6E (FFT pattern in Figure S14B). The size distribution of $BaZrO_3$ particles (determined on two different TEM cross sections of nanocomposite, Figure S15 in SI) shows a mean diameter of 13.0±0.5 nm, which indicates that the initial (3.5±0.4 nm) ZrO_2 nanocrystals have coarsened during the thermal process. The growth can be attributed to both their reactivity with Ba^{2+} and a slight degree of agglomeration in the film (Figure 6F). The latter is driven by (i) aggregation in solution (see polydispersity index, Table 1), (ii) aggregation upon deposition and drying (Figure S6) and (iii) aggregation during the thermal process. Given the large polydispersity index for short carboxylates and the observed aggregates in TEM, this is another reason for the worse performance of the short carboxylate based nanocomposites. Regarding the final $BaZrO_3$ nanoparticle size, our results obtained with copolymer stabilized nanocrystals compare favorably with literature reports using zirconium salts in YBCO solution as nanocomposite precursors. In the latter case, the final $BaZrO_3$ particles were in the order of 30 nm in diameter,[45] which is a 12 fold volume difference compared to the 13 nm particles described here.

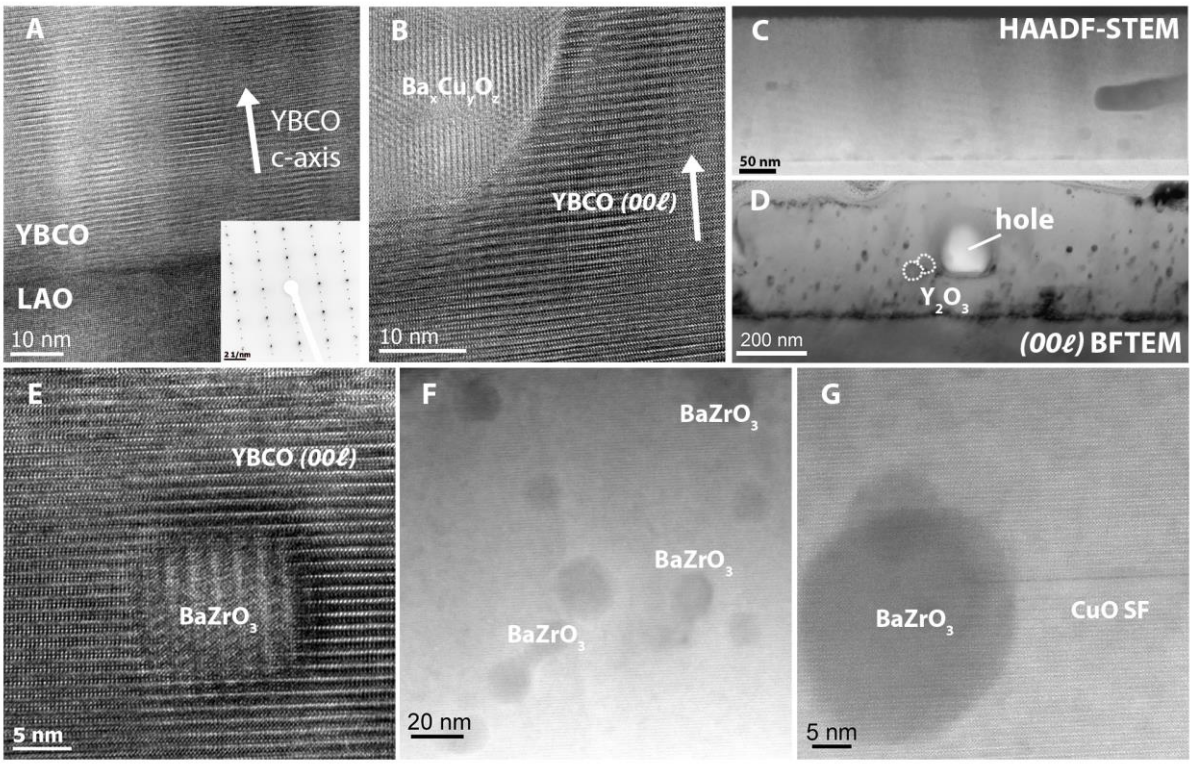

Figure 6. Undoped YBCO film: (A) HR-TEM images of the YBCO/$LaAlO_3$ interface and its diffraction pattern (inset), (B) $Ba_xCu_yO_z$ particles in the YBCO matrix and (C) High angle annular dark field (HAADF)-STEM cross sectional image. Nanocomposite film: (D) Cross-section bright field-TEM image taken with a diffraction vector $\vec{g}$ = (003). (E) HR-TEM image of randomly oriented $BaZrO_3$ particles embedded in the YBCO matrix. (F-G) HAADF-STEM Z-contrast image of YBCO-5 mol-% ZrO_2 nanocomposite. Black dots correspond to $BaZrO_3$ particles.

The $BaZrO_3$ particles are mostly randomly oriented, while YBCO remains epitaxial, thus generating incoherent interfaces which can act as nucleation centers for Y124-type intergrowths, and short Y124-type stacking faults are thought to be contributing for pinning.[46] We observed some local Y124 regions (Figure 6G) in the YBCO matrix which are possibly induced by the high amount of Y_2O_3 and non-stoichiometric amount of Ba^{2+}. The strain ε of the YBCO matrix calculated via a Williamson-Hall plot slightly increases for the nanocomposite (0.135%) compared to the undoped YBCO films (0.125%), indicating some nanostrained regions in nanocomposite matrix. Indeed, some strain is visible (black zone) in the YBCO/$LaAlO_3$ interface region. (Bright field TEM image, Figure 6D).

Optimized copolymer based nanocomposite, superconducting properties. The excellent structural properties are in accordance with high critical temperatures (T_c) of 90.5 K with a transition width ΔT_c of 1.2 K for undoped YBCO and T_c of 91.0 K with ΔT_c = 0.9 K for the nanocomposite. It is clear that the nanocrystal addition does not reduce T_c which is often observed in nanocomposite films probably due to the strain effects at the particles' interface or due to the structural defects in YBCO matrix.[47] The inductive critical current densities J_c in self-field at 77 K (voltage criterion of 50 µV) are 4.8±0.5 MA cm^{-2} for undoped YBCO (average of 6 samples) and 5.1±0.4 MA cm^{-2} for the nanocomposite (9 samples). This enhancement of J_c in self-field for the nanocomposite is probably explained by the contracted Cu-O bonds, resulting in the increase of the pair breaking energy.[48, 49] To determine the extent of vortex pinning, the magnetic field dependences of J_c were measured at 77 K with an electric field criterion of 215 µV cm^{-1} and fitted as $J_c(T,B) = A(T)B^{-\alpha}$ in the appropriate region (**Table 2**). The averaged J_c value in self-field (0 T, 77 K) for undoped YBCO is 3.3±0.3 MA cm^{-2} and decreases to 16.8±5.1 kA cm^{-2} at 1 T. The incorporation of ZrO_2 nanocrystals resulted in an increase of J_c to about 4.0±0.4 MA cm^{-2} in self-field which is a 1.2 times improvement. However, the true potential of the nanocomposite is revealed at 1 T, having a critical current of 231.1±15.6 kA cm^{-2} which is a 14 times improvement. The excellent performance of the nanocomposite is underscored by the averaged power-law exponent α at 77 K, which is about 0.74±0.03 for undoped YBCO and about 0.44±0.06 for YBCO-5 mol-% ZrO_2 nanocrystals. The smaller power law exponent for the nanocomposite indicates a less steep decay of the critical current with an increasing magnetic field and thus a better performance at high fields. From the obtained results and their low standard deviations, we conclude our approach to be highly reproducible. Often in the literature, a single champion value is reported without information on the reproducibility and we would like to present our averaging of samples as a best practice.

Table 2. The averaged critical current density in self-field and 1 T as determined from magnetic measurements, the power-law exponent α at 77 K, the critical current density (self-field) as determined from transport measurements at 77 K, the irreversibility field and maximum pinning force for undoped YBCO and YBCO-5 mol-% ZrO_2 nanocrystals.

ZrO_2	$J_{c,mag}$ (0 T), MA cm^{-2}	$J_{c,mag}$ (1 T), kA cm^{-2}	α	$J_{c,trans}$ (0 T), MA cm^{-2}	H_{irr}, T	F_P^{max}, GN m^{-3}
0 mol-%	3.3±0.3	16.8±5.1	0.74±0.03	4.65	7.5±0.1	1.6
5 mol-%	4.0±0.4	231.1±15.6	0.44±0.06	5.20	8.4±0.1	5.5

Transport current measurements of undoped YBCO and YBCO-5 mol-% ZrO_2 show a similar trend as the magnetic measurements (Table 2 and Figure 7A). The $J_c(B||c)$ curves for three different temperatures show clearly a higher performance (higher current) for the nanocomposite compared to undoped YBCO for all temperatures and all magnetic field values (Figure 7A).

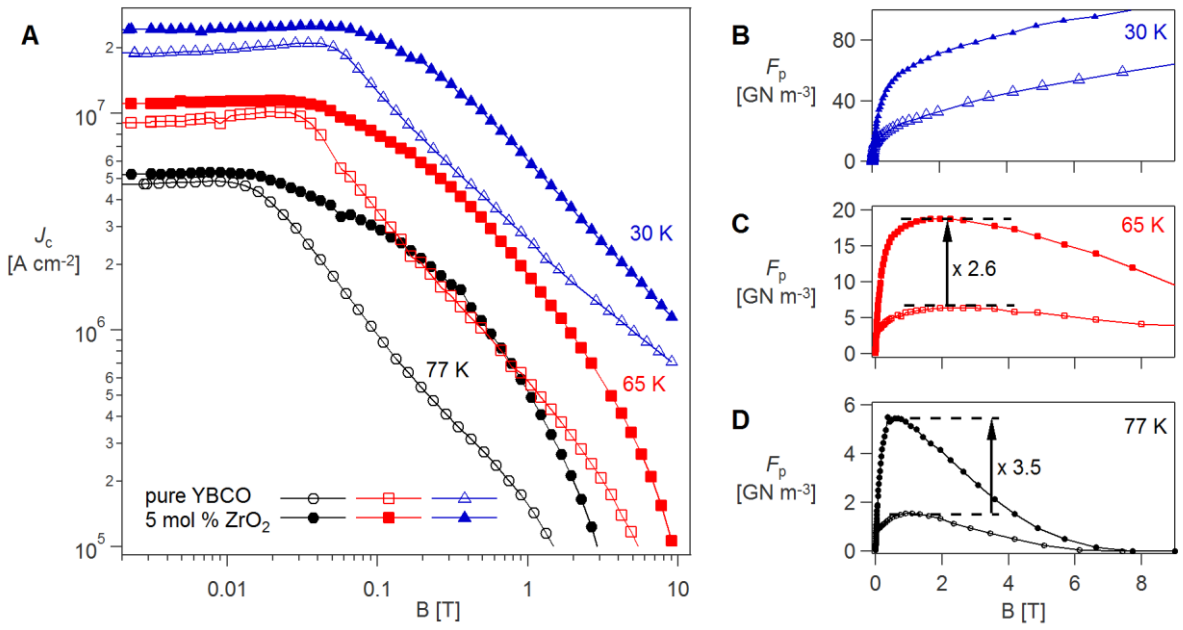

Figure 7. $J_c(B)$ for undoped and 5 mol-% ZrO_2 nanocrystals doped YBCO films at 77 K, 65 K and 30 K (A) and according pinning force curves at 30 K (B), 65 K (C) and 77 K (D).

The irreversibility field H_{irr} at 77 K increased from 7.5 T to 8.4 T by the introduction of 5 mol-% nanocrystal, and the maximum pinning force density $F_{P,max}$ more than tripled from 1.6 to 5.5 GN m^{-3} at 77 K (Table 2 and Figure 7D). This is a record pinning force value for LF-YBCO films.[50] At lower temperatures, the increase of F_P is similar but somewhat lower (Figure 7B and C). These values are slightly lower than the champion value (10-22 GN m^{-3}, 77 K) reported from the spontaneous segregation of $BaZrO_3$ particles in CSD-YBCO films[21] but improved compared to earlier reports on $BaZrO_3$ particles in LF-YBCO (3.8 GN m^{-3})[50], and our results have the additional advantage of being highly reproducible. The self-field J_c is still high for doped YBCO, so we believe that the $F_{P,max}$ can be increased by the addition of more ZrO_2 nanocrystals in the YBCO matrix if they remain small in the order of superconducting coherence length (2-4 nm for YBCO at 77 K) and agglomeration-free (to reach a higher number density of defects in YBCO matrix) without affecting the YBCO microstructure.[9]

The anisotropy of the critical current density $J_c(B,\Theta)$ was measured for a similar batch of samples at 77 K / 1 T and 30 K / 3 T (Figure 8), two typical regimes for high temperature superconductor applications, e.g. superconducting transmission cables (high temperature/low field) or motors/generators (medium temperature/medium field).[39] In both regimes, the maximum J_c at magnetic field parallel to the YBCO *ab*-plane (Θ = 90°) is approximately the same (2.1 MA cm^{-2} at 77 K / 1 T, 17 MA cm^{-2} at 30 K / 3 T, Table 3), but the overall performance is increased by nanocrystal addition in a wide angular range aside $B||ab$, and the anisotropy, i.e. the ratio of highest J_c to lowest J_c in the full $J_c(B,\Theta)$, is lowered by the nanocrystal addition.

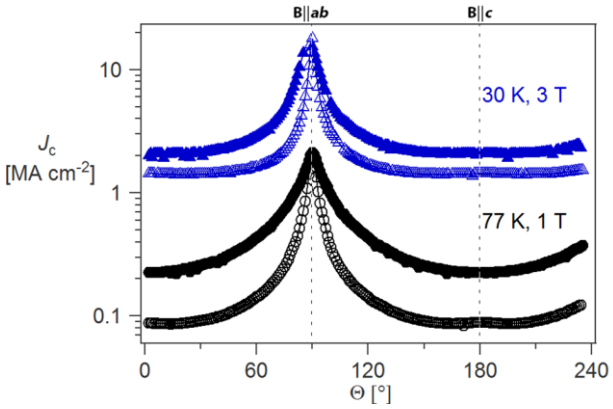

Figure 8. Anisotropy $J_c(\Theta)$ for undoped (open symbols) and 5 mol-% nanocrystal doped (closed symbols) YBCO films at 77 K / 1 T (black) and 30 K / 3 T (blue)

Table 3. J_c^{max}, J_c^{min} and Anisotropy $A = J_c^{max} / J_c^{min}$ of undoped and 5 mol-% nanocrystal doped YBCO at different temperatures and fields.

ZrO_2 nanocrystals	**undoped YBCO**			**5 mol-% nanocrystal**		
	J_c^{max}	J_c^{min}	A	J_c^{max}	J_c^{min}	A
	MA cm^{-2}		**-**	**MA cm^{-2}**		**-**
77 K / 1T	2.1	0.1	25.6	2.1	0.2	10.1
30 K / 3 T	18.0	1.4	13.4	17.1	1.9	9.0

Conclusion

Highly crystalline ZrO_2 nanocrystals were stabilized by a steric polar ligand or short carboxylates in a low-fluorine YBCO precursor solutions. From the resulting suspension, by a single coating step, we synthesized superconducting nanocomposites in a reproducible, environmentally benign way. Interestingly, nanocrystals stabilized by short carboxylate ligands resulted in poorly superconducting nanocomposites while the steric ligands lead to excellent superconductors. This is a counter-intuitive result as one would expect that the more carbon is introduced in the layer, the worse the superconductor would be. The present work has shown how to control and improve the performance of YBCO nanocomposites by understanding the stabilization and the growth of pinning-active nanocrystals in the YBCO

matrix. This approach results in a high maximum pinning force density of 5.5 GN m^{-3}, which more than tripled compared to undoped YBCO thin films. The J_c in moderate-to-high magnetic field is increased and its anisotropy is lowered by the addition of nanocrystals. Given the counter-intuitive relation between the nanocrystal surface chemistry and the final nanocomposites performance, we expect these results to be relevant for other areas of nanocomposite research as well.

Material and methods

Nanocrystal synthesis: The ZrO_2 nanocrystals are synthesized via a heating-up solvothermal method with 5 mmol $ZrCl_4$, 4 mmol Zr(OiPr) and 20 g trioctylphosphine oxide.[29] The temperature of this mixture is carefully raised until trioctylphosphine oxide is melted under Ar atmosphere. The temperature of the homogenous solution is increased to 340 °C under vigorous stirring and kept at this temperature for 2 hours. After the heating-up synthesis, the reaction mixture is cooled to 80 °C (TOPO becomes solid below 60 °C). Toluene (4:1 by volume) and acetone (1:5 by volume) is added to precipitate the nanocrystals. The precipitation is redispersed in toluene, yielding a clear suspension. In a ligand exchange step, the 1 mL ZrO_2 nanocrystal dispersion (concentration of 0.3 M) is firstly precipitated by addition of acetone (1:3 by volume). In a second step, the precipitate (obtained after centrifugation at 5000 rpm for two min) is transferred to 1 mL methanol via the addition of a 35 mg steric dispersant (a commercially available polar copolymer with phosphate groups which may be given in the form of its alkylolammonium salt, see Figure S2 for the structure) or 15 mg short carboxylate (citric acid or tartaric acid), leading to a transparent and stable nano-suspension after an ultrasonic treatment of 30-60 minutes.

Thin film deposition: The low-fluorine YBCO precursor solutions were prepared by dissolving Y-propionate, Ba-TFA and Cu-propionate in an Y:Ba:Cu ratio of 1:2:3 plus additives in methanol (CHROMASOLV®, ≥99.9% - Sigma-Aldrich). The reaction mixture is

heated to 60 °C for 30 min. Subsequently, the total metal concentration is adjusted to 1.08 M by adding methanol for undoped YBCO solutions. For 5 mol-% ZrO_2 nanocrystals doped YBCO solutions, 1 mL YBCO solution with the total metal concentration of 1.20 M is diluted by adding of 33.3 µL ZrO_2 nanocrystals (0.3 M) and further diluted with methanol to 1.08 M. Those solutions were deposited on (001)-oriented $LaAlO_3$ single crystal substrates (Crystec GmbH) by spin-coating using a spincoater model CHEMAT with a spin rate of 2000 rpm for 1 min. The substrates were ultrasonically cleaned with isopropanol followed by a heat treatment at 400 °C on a hot-plate before deposition to remove adsorbed organics prior to deposition. The deposited layers were heated at 65 °C for 3 min in order to evaporate the solvent.

The as-deposited gel films were pyrolyzed in a humidified O_2 atmosphere with the heating ramps of 3 K min^{-1} from 25 to 195 °C, 0.1 K min^{-1} to 240 °C and 5 K min^{-1} to the final temperature of 400 °C. The pyrolyzed thin films were subsequently processed to an intermediate dwell step at 640 °C for 60 min and then to 790 °C for 70 min in a flowing nitrogen atmosphere containing 100 ppm oxygen, followed by an oxygenation treatment at 450 °C in flowing dry oxygen for 2 h to convert the tetragonal YBCO phase to the superconducting orthorhombic phase.

Nanocrystal characterization: The dried metal oxide nanocrystal powders were characterized via X-ray diffraction (XRD) at a Thermo Scientific ARL X'tra X-ray diffractometer (Cu-K_α radiation) with Rietveld quantitative refinement to determine the crystal phase and its crystallinity degree. Dynamic light scattering analysis was performed on a Malvern Nano ZS in backscattering mode (173°). High-resolution TEM images were taken on a JEOL JEM-2200FS TEM equipped with an objective lens C_s corrector. To evaluate the temperature dependency of the decomposition of pure ligands and ligands capped nanocrystals in the LF-YBCO precursor during the pyrolysis, thermogravimetrical analysis with differential thermal

analysis were carried out using a Netzsch Model STA 449 F3 Jupiter. X-ray photoelectron spectroscopy measurements were carried out using an S-Probe monochromatized spectrometer from Surface Science Instruments with an Al-K_α X-ray monochromatic source (1486.6 eV, more details in SI). NMR measurements were recorded on a Bruker Avance III Spectrometer operating at a ^{1}H frequency of 500.13 MHz and equipped with a BBI-Z probe. The sample temperature was set to 298.2 K. One dimensional (1D) ^{1}H and 2D NOESY spectra were acquired using standard pulse sequences from the Bruker library. NOESY mixing time was set to 300 ms and 2048 data points in the direct dimension for 512 data points in the indirect dimension were typically sampled, with the spectral width set to 11.5 ppm. For 2D processing, the spectra were zero filled until a 4096×2048 real data matrix. Before Fourier transformation, the 2D spectra were multiplied with a squared cosine bell function in both dimensions. Diffusion measurements (2D DOSY) were performed using a double stimulated echo sequence for convection compensation and with monopolar gradient pulses. Smoothed rectangle gradient pulse shapes were used throughout. The gradient strength was varied linearly from 2-95 % of the probe's maximum value (calibrated at 50.2 G cm^{-1}) in 64 steps, with the gradient pulse duration and diffusion delay optimized to ensure a final attenuation of the signal in the final increment of less than 10 % relative to the first increment.

Texture characterization: Texture and phase composition of the YBCO thin films were characterized by means of XRD on a Bruker D8 diffractometer (Cu-K_α). θ-2θ scans were measured between 2θ = 25° and 46° with a step width of 0.05° to analyse the purity of the thin films. In addition, θ-2θ with a finer step width of 0.02° and rocking curve scans on the YBCO (006) (2θ = 46.5°) peak were performed. The full width at half maximum (FWHM) values are determined by fitting a Gaussian to the experimental data. The (biaxial) crystal growth direction was determined by pole figure scans for YBCO (103) (2θ = 32.6°, Ψ = 45.0°).

Microstructural characterization: Structural properties were characterized with an FEI Nova 600 Nanolab Dual Beam FIB-SEM and a JEOL JEM 2200-FS TEM. For the TEM measurements, a cross-sectional lamella was cut via the FIB *in-situ* lift out procedure with an Omniprobe™ extraction needle and top cleaning. Crystallographic information was obtained by high-resolution TEM and high-angle annular dark field (HAADF) STEM. Foreign phases in the YBCO matrix were determined via energy dispersive X-ray spectroscopy in HAADF-STEM. The image processing software *ImageJ* was used for the statistical measurement of nanocrystals in cross-sectional areas.

Electrical characterization: The self-field critical current density J_c was evaluated inductively with a THEVA Cryoscan at 77 K with a voltage criterion of 50 µV (corresponding to an electric field criterion (E_c) of 1 µV cm^{-1} in transport measurements). The field dependence of J_c was determined in magnetization and transport measurements. Magnetic J_c was calculated from DC magnetization curves at 10 K and 77 K ($\mu_0 B$ = -8 … +8 T, E_c = 215 µV cm^{-1}) on a Quantum Design Magnetic Property Measurement System using the Bean critical state model.[51] The critical temperature T_c was defined as the onset temperature of the in-phase component of the AC-magnetization at zero-field in the range of 10-100 K. The width of the magnetic transition was calculated as $\Delta T_c = T_{c,90} - T_{c,10}$.Transport critical current densities were measured in maximum Lorentz force configuration on laser-cut bridges (l = 800 µm, w ~ 15-20 µm, E_c = 1 µV cm^{-1}) at magnetic fields up to 9 T in a Quantum Design Physical Property Measurements System. The irreversibility field H_{irr} was estimated with constant J_c criterion (50 A/cm^2) and cross-checked by the condition $n \rightarrow 1$ for $H \rightarrow H_{irr}$ (n being the exponent in $E(J) \sim J^n$ near J_c). Angular-dependent $J_c(B,\Theta)$ measurements were performed by rotating the sample with steps of 2° between 0° and 240° (with $B||c_{YBCO}$ at Θ = 0° and $B||ab$ at 90°) at 77 K/1 T and 30 K/3 T.

Supporting Information

The Supporting Information is available free of charge on the ACS Publications website at

DOI:

Rietveld quantitative analysis of ZrO_2 particles, structure of the steric dispersant, DLS measurement of tartaric acid in methanol, stability of the YBCO precursor solution with 30 mol-% steric dispersant capped ZrO_2 nanocrystals, NMR analysis of the copolymer stabilized nanocrystals, Optical characterization and XPS measurements of YBCO thin films after pyrolysis, TGA measurements of pure ligands and precursors with ligands, YBCO (103) pole figure, XRD φ, rocking (ω) curves scans of YBCO layer after thermal process. Fast Fourier transformation pattern of $Ba_xCu_yO_z$ and $BaZrO_3$ particles. Fitted curves of preformed ZrO_2 nanocrystals and $BaZrO_3$ particles in YBCO layer.

Author information

Corresponding Authors

*E-mail: Isabel.VanDriessche@UGent.be

Notes

The authors declare no competing financial interest.

Acknowledgements

The authors would like to thank Olivier Janssens for XRD analysis, Dr. Els Bruneel for XPS analysis and Rainer Nast for the laser-structuring of nanobridges. This work was financially supported by a BOF research fund of Ghent University (BOF11/DOC/286) and Eurotapes, a collaborative project funded by the European Union's Seventh Framework Program (EU-FP7 NMP-LA-2012-280432). JDR thanks FWO Vlaanderen, Fulbright and B.A.E.F. for fellowships. PP and HH wish to thank the Jenny and Antti Wihuri Foundation for financial support.

References

(1) Malozemoff, A. Electric power grid application requirements for superconductors. *MRS bull.* **2011**, *36*, 601-607.

(2) Kang, S.; Goyal, A.; Li, J.; Gapud, A. A.; Martin, P. M.; Heatherly, L.; Thompson, J. R.; Christen, D. K.; List, F. A.; Paranthaman, M.; Lee, D. F. High-Performance High-T_c Superconducting Wires. *Science* **2006**, *311*, 1911-1914.

(3) Puig, T.; Gutiérrez, J.; Pomar, A.; Llordés, A.; Gazquez, J.; Ricart, S.; Sandiumenge, F.; Obradors, X. Vortex pinning in chemical solution nanostructured YBCO films. *Supercond. Sci. Technol.* **2008**, *21*, 034008.

(4) Harada, T.; Yoshida, K. The effect of rare-earth substitution at the Ba site on the flux pinning properties of $Y(Ba_{2-x}R_x)Cu_3O_{7-x}$(for R = La, Pr, and Nd). *Physica C* **2003**, *391*, 1-7.

(5) Civale, L. Vortex pinning and creep in high-temperature superconductors with columnar defects. *Supercond. Sci. Technol.* **1997**, *10*, A11-A28.

(6) Develos-Bagarinao, K.; Wimbush, S.; Matsui, H.; Yamaguchi, I.; MacManus-Driscoll, J. Enhanced flux pinning in MOD $YBa_2Cu_3O_{7-\delta}$ films by ion milling through anodic alumina templates. *Supercond. Sci. Technol.* **2012**, *25*, 065005.

(7) Wee, S. H.; Zuev, Y. L.; Cantoni, C.; Goyal, A. Engineering nanocolumnar defect configurations for optimized vortex pinning in high temperature superconducting nanocomposite wires. *Sci. Rep.* **2013**, *3*, 2310.

(8) Obradors, X.; Puig, T.; Palau, A.; Pomar, A.; Sandiumenge, F.; Mele, P.; Matsumoto, K., Nanostructured Superconductors with Efficient Vortex Pinning. In *Comprehensive Nanoscience and Technology*, Andrews, D. L.; Scholes, G. D.; Wiederrecht, G. P., Eds. Academic Press: Oxford, 2011; pp 303-349.

(9) Haugan, T.; Barnes, P.; Wheeler, R.; Meisenkothen, F.; Sumption, M. Addition of nanoparticle dispersions to enhance flux pinning of the $YBa_2Cu_3O_{7-x}$ superconductor. *Nat. Mater.* **2004**, *430*, 867-870.

(10) Baca, F. J.; Haugan, T. J.; Barnes, P. N.; Holesinger, T. G.; Maiorov, B.; Lu, R.; Wang, X.; Reichart, J. N.; Wu, J. Z. Interactive Growth Effects of Rare-Earth Nanoparticles on Nanorod Formation in $YBa_2Cu_3O_x$ Thin Films. *Adv. Funct. Mater.* **2013**, *23*, 4826-4831.

(11) Hänisch, J.; Cai, C.; Stehr, V.; Hühne, R.; Lyubina, J.; Nenkov, K.; Fuchs, G.; Schultz, L.; Holzapfel, B. Formation and pinning properties of growth-controlled nanoscale precipitates in $YBa_2Cu_3O_{7-\delta}$/transition metal quasi-multilayers. *Supercond. Sci. Technol.* **2006**, *19*, 534-540.

(12) Zhao, R.; Li, W.; Lee, J. H.; Choi, E. M.; Liang, Y.; Zhang, W.; Tang, R.; Wang, H.; Jia, Q.; MacManus-Driscoll, J. L. Precise Tuning of $(YBa_2Cu_3O_{7-\delta})_{1-x}$:$(BaZrO_3)_x$ Thin Film Nanocomposite Structures. *Adv. Funct. Mater.* **2014**, *24*, 5240-5245.

(13) Opherden, L.; Sieger, M.; Pahlke, P.; Hühne, R.; Schultz, L.; Meledin, A.; Van Tendeloo, G.; Nast, R.; Holzapfel, B.; Bianchetti, M. Large pinning forces and matching effects in $YBa_2Cu_3O_{7-\delta}$ thin films with $Ba_2Y(Nb/Ta)O_6$ nano-precipitates. *Sci. Rep.* **2016**, *6*, 21188

(14) Obradors, X.; Puig, T.; Pomar, A.; Sandiumenge, F.; Mestres, N.; Coll, M.; Cavallaro, A.; Romà, N.; Gázquez, J.; González, J. C.; Castaño, O.; Gutierrez, J.; Palau, A.; Zalamova, K.; Morlens, S.; Hassini, A.; Gibert, M.; Ricart, S.; Moretó, J. M.; Piñol, S.; Isfort, D.; Bock, J. Progress towards all-chemical superconducting $YBa_2Cu_3O_7$-coated conductors. *Supercond. Sci. Technol.* **2006**, *19*, S13-S26.

(15) Feys, J.; Vermeir, P.; Lommens, P.; Hopkins, S. C.; Granados, X.; Glowacki, B. A.; Baecker, M.; Reich, E.; Ricard, S.; Holzapfel, B. Ink-jet printing of $YBa_2Cu_3O_7$ superconducting coatings and patterns from aqueous solutions. *J. Mater. Chem.* **2012**, *22*, 3717-3726.

(16) Rijckaert, H.; De Roo, J.; Roeleveld, K.; Pollefeyt, G.; Bennewitz, J.; Bäcker, M.; Lynen, F.; De Keukeleere, K.; Van Driessche, I. Microwave-assisted $YBa_2Cu_3O_7$ precursors: A fast and reliable method towards chemical precursors for superconducting films. *J. Am. Ceram. Soc* **2017**, *100*, 2407–2418.

(17) Lei, L.; Zhao, G.; Xu, H.; Wu, N.; Chen, Y. Influences of Y_2O_3 nanoparticle additions on the microstructure and superconductivity of YBCO films derived from low-fluorine solution. *Mater. Chem. Phys.* **2011**, *127*, 91-94.

(18) Ye, S.; Suo, H.; Wu, Z.; Liu, M.; Xu, Y.; Ma, L.; Zhou, M. Preparation of solution-based YBCO films with $BaSnO_3$ particles. *Physica C Supercond* **2011**, *471*, 265-269.

(19) Erbe, M.; Hänisch, J.; Hühne, R.; Freudenberg, T.; Kirchner, A.; Molina-Luna, L.; Damm, C.; Van Tendeloo, G.; Kaskel, S.; Schultz, L. $BaHfO_3$ artificial pinning centres in TFA-MOD-derived YBCO and GdBCO thin films. *Supercond. Sci. Technol.* **2015**, *28*, 114002.

(20) Ding, F.; Gu, H.; Zhang, T.; Wang, H.; Qu, F.; Qiu, Q.; Dai, S.; Peng, X.; Cao, J.-L. Strong enhancement flux pinning in MOD-$YBa_2Cu_3O_{7-x}$ films with self-assembled $BaTiO_3$ nanocolumns. *Appl. Surf. Sci.* **2014**, *314*, 622-627.
(21) Gutierrez, J.; Llordes, A.; Gazquez, J.; Gibert, M.; Roma, N.; Ricart, S.; Pomar, A.; Sandiumenge, F.; Mestres, N.; Puig, T. Strong isotropic flux pinning in solution-derived $YBa_2Cu_3O_{7-x}$ nanocomposite superconductor films. *Nat. Mater.* **2007**, *6*, 367-373.
(22) Coll, M.; Guzman, R.; Garcés, P.; Gazquez, J.; Rouco, V.; Palau, A.; Ye, S.; Magen, C.; Suo, H.; Castro, H.; Puig, T.; Obradors, X. Size-controlled spontaneously segregated Ba_2YTaO_6 nanoparticles in $YBa_2Cu_3O_7$ nanocomposites obtained by chemical solution deposition. *Supercond. Sci. Technol.* **2014**, *27*, 044008.
(23) Martinez-Julian, F.; Ricart, S.; Pomar, A.; Coll, M.; Abellán, P.; Sandiumenge, F.; Casanove, M.-J.; Obradors, X.; Puig, T.; Pastoriza-Santos, I. Chemical Solution Approaches to $YBa_2Cu_3O_7$-Au Nanocomposite Superconducting Thin Films. *J. Nanosci. Nanotechnol.* **2011**, *11*, 3245-3255.
(24) Cayado, P.; De Keukeleere, K.; Garzón, A.; Perez-Mirabet, L.; Meledin, A.; De Roo, J.; Vallés, F.; Mundet, B.; Rijckaert, H.; Pollefeyt, G.; Coll, M.; Ricart, S.; Palau, A.; Gazquez, J.; Ros, J.; Van Tendeloo, G.; Van Driessche, I.; Puig, T.; Obradors, X. Epitaxial $YBa_2Cu_3O_{7-x}$ nanocomposite thin films from colloidal solutions. *Supercond. Sci. Technol.* **2015**, *28*, 124007.
(25) De Keukeleere, K.; Cayado, P.; Meledin, A.; Vallès, F.; De Roo, J.; Rijckaert, H.; Pollefeyt, G.; Bruneel, E.; Palau, A.; Coll, M.; Ricart, S.; Van Tendeloo, G.; Puig, T.; Obradors, X.; Van Driessche, I. Superconducting $YBa_2Cu_3O_{7-\delta}$ Nanocomposites Using Preformed ZrO_2 Nanocrystals: Growth Mechanisms and Vortex Pinning Properties. *Adv. Electr. Mater.* **2016**, *2*, 1600161.
(26) Llordes, A.; Zalamova, K.; Ricart, S.; Palau, A.; Pomar, A.; Puig, T.; Hardy, A.; Van Bael, M.; Obradors, X. Evolution of metal-trifluoroacetate precursors in the thermal decomposition toward high-performance $YBa_2Cu_3O_7$ superconducting films. *Chem. Mater.* **2010**, *22*, 1686-1694.
(27) Palmer, X.; Pop, C.; Eloussifi, H.; Villarejo, B.; Roura, P.; Farjas, J.; Calleja, A.; Palau, A.; Obradors, X.; Puig, T. Solution design for low-fluorine trifluoroacetate route to $YBa_2Cu_3O_7$ films. *Supercond. Sci. Technol.* **2015**, *29*, 024002.
(28) De Roo, J.; Coucke, S.; Rijckaert, H.; De Keukeleere, K.; Sinnaeve, D.; Hens, Z.; Martins, J. C.; Van Driessche, I. Amino Acid-Based Stabilization of Oxide Nanocrystals in Polar Media: From Insight in Ligand Exchange to Solution ^{1}H NMR Probing of Short-Chained Adsorbates. *Langmuir* **2016**, *32*, 1962-1970.
(29) Joo, J.; Yu, T.; Kim, Y. W.; Park, H. M.; Wu, F.; Zhang, J. Z.; Hyeon, T. Multigram scale synthesis and characterization of monodisperse tetragonal zirconia nanocrystals. *J. Am. Chem. Soc.* **2003**, *125*, 6553-6557.
(30) Ren, S.; Chang, L.-Y.; Lim, S.-K.; Zhao, J.; Smith, M.; Zhao, N.; Bulovic, V.; Bawendi, M.; Gradecak, S. Inorganic–organic hybrid solar cell: bridging quantum dots to conjugated polymer nanowires. *Nano Lett.* **2011**, *11*, 3998-4002.
(31) Kim, P.; Doss, N. M.; Tillotson, J. P.; Hotchkiss, P. J.; Pan, M.-J.; Marder, S. R.; Li, J.; Calame, J. P.; Perry, J. W. High energy density nanocomposites based on surface-modified $BaTiO_3$ and a ferroelectric polymer. *ACS nano* **2009**, *3*, 2581-2592.
(32) Ramesh, R.; Spaldin, N. A. Multiferroics: progress and prospects in thin films. *Nat. Mater.* **2007**, *6*, 21-29.
(33) Shan, C.; Yang, H.; Han, D.; Zhang, Q.; Ivaska, A.; Niu, L. Graphene/AuNPs/chitosan nanocomposites film for glucose biosensing. *Biosens. Bioelectron.* **2010**, *25*, 1070-1074.
(34) Guiton, B. S.; Davies, P. K. Nano-chessboard superlattices formed by spontaneous phase separation in oxides. *Nat. Mater.* **2007**, *6*, 586-591.
(35) Bogle, K. A.; Anbusathaiah, V.; Arredondo, M.; Lin, J.-Y.; Chu, Y.-H.; O'Neill, C.; Gregg, J. M.; Castell, M. R.; Nagarajan, V. Synthesis of epitaxial metal oxide nanocrystals via a phase separation approach. *ACS nano* **2010**, *4*, 5139-5146.
(36) Komarneni, S. Nanocomposites. *J. Mater. Chem. A* **1992**, *2*, 1219-1230.
(37) Moya, J. S.; Lopez-Esteban, S.; Pecharroman, C. The challenge of ceramic/metal microcomposites and nanocomposites. *Prog. Mater. Sci.* **2007**, *52*, 1017-1090.

(38) Fritzinger, B.; Moreels, I.; Lommens, P.; Koole, R.; Hens, Z.; Martins, J. C. In situ observation of rapid ligand exchange in colloidal nanocrystal suspensions using transfer NOE nuclear magnetic resonance spectroscopy. *J. Am. Chem. Soc* **2009**, *131*, 3024-3032.
(39) Obradors, X.; Puig, T. Coated conductors for power applications: materials challenges. *Supercond. Sci. Technol.* **2014**, *27*, 044003.
(40) Zalamova, K.; Romà, N.; Pomar, A.; Morlens, S.; Puig, T.; Gázquez, J.; Carrillo, A. E.; Sandiumenge, F.; Ricart, S.; Mestres, N.; Obradors, X. Smooth Stress Relief of Trifluoroacetate Metal-Organic Solutions for $YBa_2Cu_3O_7$ Film Growth. *Chem. Mater.* **2006**, *18*, 5897-5906.
(41) Zeng, J.; Lian, J.; Wang, L.; Chou, P.; Ignatiev, A. HRTEM characterization of $YBa_2Cu_3O_{7-\delta}$ thick films on $LaAlO_3$ substrates. *Physica C Supercond.* **2004**, *405*, 127-132.
(42) Viswanathan, S. K.; Gapud, A. A.; Varela, M.; Abiade, J. T.; Christen, D. K.; Pennycook, S. J.; Kumar, D. Enhancement of critical current density of $YBa_2Cu_3O_{7-\delta}$ thin films by self-assembly of Y_2O_3 nanoparticulates. *Thin Solid Films* **2007**, *515*, 6452-6455.
(43) Mele, P.; Guzman, R.; Gazquez, J.; Puig, T.; Obradors, X.; Saini, S.; Yoshida, Y.; Mukaida, M.; Ichinose, A.; Matsumoto, K. High pinning performance of $YBa_2Cu_3O_{7-x}$ films added with Y_2O_3 nanoparticulate defects. *Supercond. Sci. Technol.* **2014**, *28*, 024002.
(44) Wimbush, S. C.; Li, M.; Vickers, M. E.; Maiorov, B.; Feldmann, D. M.; Jia, Q.; MacManus-Driscoll, J. L. Interfacial Strain-Induced Oxygen Disorder as the Cause of Enhanced Critical Current Density in Superconducting Thin Films. *Adv. Funct. Mater.* **2009**, *19*, 835-841.
(45) Llordes, A.; Palau, A.; Gazquez, J.; Coll, M.; Vlad, R.; Pomar, A.; Arbiol, J.; Guzman, R.; Ye, S.; Rouco, V.; Sandiumenge, F.; Ricart, S.; Puig, T.; Varela, M.; Chateigner, D.; Vanacken, J.; Gutierrez, J.; Moshchalkov, V.; Deutscher, G.; Magen, C.; Obradors, X. Nanoscale strain-induced pair suppression as a vortex-pinning mechanism in high-temperature superconductors. *Nat. Mater.* **2012**, *11*, 329-336.
(46) Llordés, A.; Palau, A.; Gázquez, J.; Coll, M.; Vlad, R.; Pomar, A.; Arbiol, J.; Guzmán, R.; Ye, S.; Rouco, V.; Sandiumenge, F.; Ricart, S.; Puig, T.; Varela, M.; Chateigner, D.; Vanacken, J.; Gutiérrez, J.; Moshchalkov, V.; Deutscher, G.; Magen, C.; Obradors, X. Nanoscale strain-induced pair suppression as a vortex-pinning mechanism in high-temperature superconductors. *Nat. Mater.* **2012**, *11*, 329-336.
(47) Huhtinen, H.; Schlesier, K.; Paturi, P. Growth and c-axis flux pinning of nanostructured YBCO/BZO multilayers. *Supercond. Sci. Technol.* **2009**, *22*, 075019.
(48) Deutscher, G. The role of Cu-O bond length fluctuations in the high temperature superconductivity mechanism. *J. Appl. Phys.* **2012**, *111*, 112603.
(49) Lei, L.; Liu, L.; Wang, X.; Wang, S.; Jia, J.; Zhao, G.; Wu, C.; Jin, L.; Li, C.; Zhang, P. Strongly improved current-carrying capacity induced by nanoscale lattice strains in $YBa_2Cu_3O_{7-\delta}$–$Ba_{0.7}Sr_{0.3}TiO_3$ composite films derived from chemical solution deposition. *J. Mater. Chem. C* **2016**, *4*, 1392-1397.
(50) Petrisor Jr, T.; Mos, R.; Nasui, M.; Gabor, M.; Augieri, A.; Celentano, G.; De Felicis, D.; Bemporad, E.; Ciontea, L.; Petrisor, T. The Vortex Path Model Analysis of the Field Angle Dependence of the Critical Current Density in Nanocomposite $YBa_2Cu_3O_{7-x}$–$BaZrO_3$ Films Obtained by Low Fluorine Chemical Solution Deposition. *J Supercond Nov Magn* **2014**, *27*, 2493-2500.
(51) Gyorgy, E.; Van Dover, R.; Jackson, K.; Schneemeyer, L.; Waszczak, J. Anisotropic critical currents in $Ba_2YCu_3O_7$ analyzed using an extended Bean model. *Appl. Phys. Lett.* **1989**, *55*, 283-285.

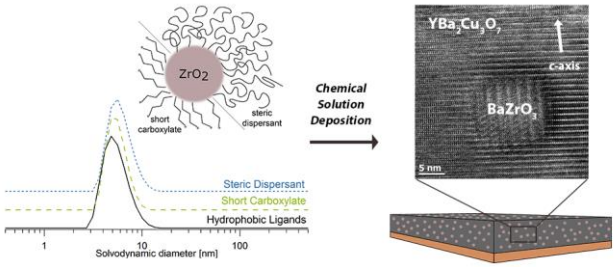
ZrO2
short carboxylate
steric dispersant
Steric Dispersant
Short Carboxylate
Hydrophobic Ligands
1
10
100
Solvodynamic diameter [nm]
Chemical Solution Deposition
YBa2Cu3O7
c-axis
BaZrO3
5 nm